Slow light in flight imaging

Kali Wilson,[1,*] Bethany Little,[2] Genevieve Gariepy,[1] Robert Henderson,[3] John Howell,[2] and Daniele Faccio[1,†]
[1]*Institute of Photonics and Quantum Sciences, Heriot-Watt University, Edinburgh EH14 4AS, United Kingdom*
[2]*Department of Physics and Astronomy, University of Rochester, Rochester, New York 14627, USA*
[3]*Institute for Micro and Nano Systems, University of Edinburgh, Alexander Crum Brown Road, Edinburgh EH9 3FF, United Kingdom*
(Received 20 October 2016; published 15 February 2017)

Slow-light media are of interest in the context of quantum computing and enhanced measurement of quantum effects, with particular emphasis on using slow light with single photons. We use light-in-flight imaging with a single-photon avalanche diode camera array to image *in situ* pulse propagation through a slow-light medium consisting of heated rubidium vapor. Light-in-flight imaging of slow-light propagation enables direct visualization of a series of physical effects, including simultaneous observation of spatial pulse compression and temporal pulse dispersion. Additionally, the single-photon nature of the camera allows for observation of the group velocity of single photons with measured single-photon fractional delays greater than 1 over 1 cm of propagation.

DOI: 10.1103/PhysRevA.95.023830

I. INTRODUCTION

Slow light has been proposed and studied as a resource for building quantum networks; carefully controlled transmission of quantum states of light [1,2], tuneable delay lines [3,4] with fast reconfiguration rates [5] and spectral resolution [6], and tuneable delay of entangled images [7] are just a few examples. More recently, slow light has been exploited to enhance measurement, either through improving the sensitivity of interferometers [8] or by enhancing effects that would normally be too small to observe, such as rotary photon drag [9] and Fresnel light dragging [10,11], or the proposed observation of gravitational deflection of classical light [12].

In the context of quantum optics and communications, there is significant interest in the use of slow light as an optical buffer where signals can be stored and resynchronized. Large fractional delays for single photons are essential for such quantum buffers and memories. Slow group velocities ($v_g \sim 0.003c$) for single photons have been demonstrated previously [1] in an electromagnetically induced transparency (EIT) configuration with narrow pulse bandwidths (of the order of MHz), required to fit within the EIT window, and correspondingly large temporal pulse widths of the order of 150 ns. Such long pulse widths limit the overall fractional pulse delay to $f_D = \Delta t/\tau < 1$, where Δt is the net pulse delay and τ is the temporal pulse width [13]. Progress has been made in the high pulse intensity (many-photon) regime [14,15], with $f_D \sim 72$ reported by Chen *et al.* [15]. However, such EIT schemes are still limited to narrow bandwidth pulses and have not yet been applied to single photons.

Another promising slow-light scheme employs an absorption doublet in a hot atomic vapor, such as rubidium or cesium. In this scenario, the frequency of the light is tuned in the region between two absorption resonances with no need for an additional pump beam as required for EIT. Moreover, large bandwidths of the order of 1–10 GHz are available so that short pulses and large fractional pulse delays $f_D > 10$ are possible both for classical pulses [5] and for single photons [4].

In this work, we take advantage of light-in-flight imaging techniques in conjunction with a camera comprised of an array of single-photon avalanche diodes (SPAD camera) [16–18] to simultaneously detect *in situ* both the spatial compression and the temporal dispersion of a pulse of light traveling through a slow-light medium. Here the medium consists of a hyperfine absorption doublet in hot Rb vapor. Generally, slow-light effects have been characterized as the net effect of a pulse propagating through the slow-light medium, i.e., as a pulse delay time measured with a fast photodiode at the output of the medium [3]. *In situ* imaging of slow light therefore provides a different approach for studying the physics of such media and enables observation of pulse propagation dynamics as well as single-photon dynamics as a result of the single-photon sensitivity of the camera. Indeed, we observe a significant delay, of the order of nanoseconds, in the detection of the photons scattered as the pulse enters the slow-light medium. This lag in scattered-photon arrival time is a direct visualization of the slowing down of the single-photon group velocity. The pulses used here had a temporal full width at half maximum (FWHM) of $\tau \sim 1$ ns, corresponding to a frequency FWHM of $\Delta\nu \sim 440$ MHz, with measured group velocities as low as $v_g \sim 0.006c$. At these low group velocities, we observe a full fractional pulse delay of up to $f_D \sim 40$ over 7 cm of propagation, and $f_D \sim 5$ for the scattered single photons, which propagate through ~1 cm of Rb vapor prior to exiting the cell en route to the camera.

II. SLOW-LIGHT MEDIUM

We work in the slow-light region of the dispersion curve in between the ^{85}Rb D_1 hyperfine transitions. Following Camacho *et al.* [3], we approximate the real n' and imaginary n'' components of the index of refraction $n = n' + in''$ to be

$$n' \approx 1 + \frac{A\delta}{{\omega_0}^2} + \frac{3A\delta^3}{{\omega_0}^4}, \tag{1}$$

$$n'' \approx \frac{A\gamma}{{\omega_0}^2} + \frac{3A\gamma\delta^2}{{\omega_0}^4}. \tag{2}$$

Here, A is a constant that characterizes the strength of the susceptibility, $\omega_0 = (\omega_2 - \omega_1)/2 \sim 2\pi \times 1.5$ GHz is half the

*k.wilson@hw.ac.uk
†d.faccio@hw.ac.uk

separation between the two hyperfine transitions comprising the doublet, δ is the detuning from the midpoint between the two transitions, and $\gamma = \pi \times 5.75$ MHz is the half width at half maximum of the transitions. For the above approximation to be valid, we assume small detuning $|\delta| << \omega_0$, relatively large pulse bandwidths $1/\tau > \gamma$, and parameters of the medium that satisfy the condition $\omega_0 >> \gamma$, with a susceptibility $\chi << 1$. Within these reasonable assumptions and evaluating the absorption coefficient $\alpha = 2\omega n''/c$ in between the two resonances, we have

$$\alpha_{\delta=0} = \frac{2\omega A\gamma}{c{\omega_0}^2}, \tag{3}$$

where $\omega = (\omega_1 + \omega_2)/2 + \delta$, and c is the vacuum speed of light. We can then define the group velocity,

$$v_g \approx \frac{c}{\omega(dn'/d\delta)} \approx \frac{2\gamma}{\alpha_{\delta=0}}, \tag{4}$$

and write the group velocity in terms of the optical depth $D = \alpha L$ of the Rb vapor,

$$v_g \approx \frac{2\gamma L}{D_{\delta=0}}. \tag{5}$$

Since the optical depth depends on temperature, we tune the group velocity by varying the temperature of the Rb vapor, with hotter temperature corresponding to slower group velocity.

III. EXPERIMENTAL LAYOUT

Our experimental slow-light setup is shown in Fig. 1(a). We use a Photodigm distributed Bragg reflector laser diode with wavelength $\lambda = 795$ nm tuned to the middle of the ^{85}Rb D_1 hyperfine doublet, corresponding to $\delta \sim 0$ GHz, as shown in the representative transmission spectra in Fig. 1(b). The laser wavelength is tuned via current and temperature, and is sufficiently stable without the need for servo-locking. We use a fiber-coupled electro-optical modulator (EOM) operating at 25 MHz with a 2% duty cycle to modulate the laser intensity, creating nearly Gaussian pulses with a temporal FWHM of $\tau \sim 1$ ns, corresponding to a frequency FWHM of $\Delta\nu \sim 440$ MHz, and pulse energy of the order of 1 pJ. The pulses travel through a heated glass cell containing Rb vapor, as shown in Fig. 1(a). The Rb vapor cell is enclosed in a transparent, outer, insulating glass cell [not shown in Fig. 1(a) for simplicity]. We use two different vapor cells, with outer lengths of $L = 7.18$ cm and $L = 30$ cm, respectively. A photodiode placed after the Rb vapor cell is used to capture transmission spectra and for preliminary characterization of the pulse shape. Figure 1(b) shows a representative transmission spectrum with the 7.18 cm cell heated to $T \sim 150\,^{\circ}$C, and $D \sim 2.5$ at $\delta \sim 0$ GHz (orange trace). The transmission spectrum for a room-temperature gas, $T \sim 20\,^{\circ}$C is given for comparison (blue trace).

IV. LIGHT-IN-FLIGHT IMAGING

Following the method of Gariepy *et al.* [16], we operate a camera consisting of a 32×32 array of single-photon avalanche diodes (SPADs) in the time-correlated, single-photon counting mode, with the SPADs triggered off of the

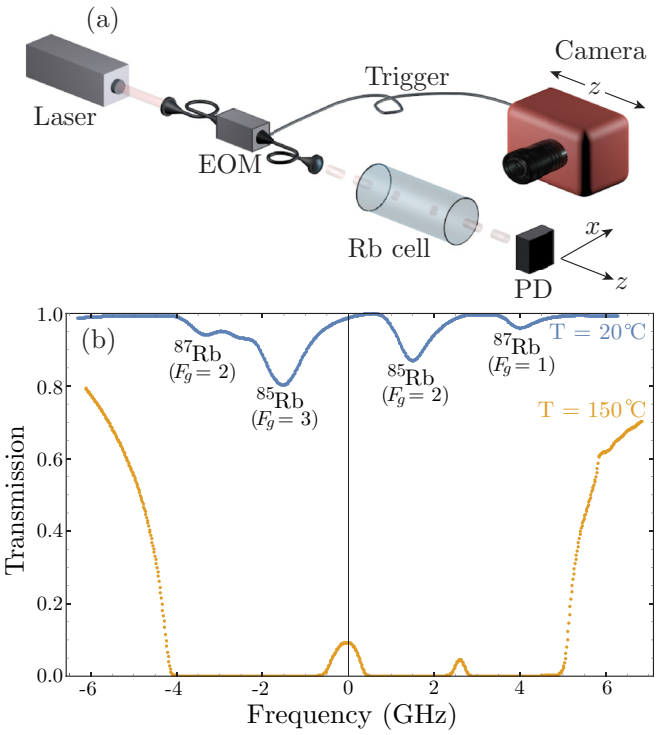

FIG. 1. (a) Experimental setup (not to scale). A fiber-coupled electro-optical modulator (EOM) chops the laser beam into pulses, which propagate through the Rb vapor cell, from left to right along the z axis. The Rb vapor cell is heated and enclosed in a transparent, outer, insulating glass cell (not shown for simplicity). The fast photodiode (PD) is used to measure the transmission spectra shown in (b). The SPAD camera is set up to capture light scattered by the Rb vapor along the x axis. The camera has a 5 cm field of view (resolution of $\delta z = 1.6$ mm) and is scanned along the z axis by 4 cm increments. (b) Transmission spectra for the $L = 7.18$ cm cell. A temperature of $T \sim 150\,^{\circ}$C corresponds to $D \sim 2.5$ at $\delta \sim 0$ GHz, with a group velocity $v_g = c/183$, determined from the SPAD data. The room-temperature transmission spectrum, $T \sim 20\,^{\circ}$C, is provided for reference.

EOM. We detect photons scattered by the slow-light medium that travel out of the medium perpendicular to the direction of pulse propagation, along the x axis, as shown in Fig. 1(a). The scattered light is imaged onto the SPAD camera with a standard camera lens (Sigma 18-35 mm F1.8 DC HSM) with an f-number of 1.8 and a focal length of 18 cm, resulting in a 5 cm field of view in the plane of the pulse propagation. We translate the camera along the z pulse propagation axis by increments of $\Delta z_{\text{cam}} = 4$ cm so as to scan the pulse propagation along the entire length of the Rb cell. The full pulse propagation is then stitched together from the set of scans. We also acquired a reference scan for a pulse propagating in air at $v_g \sim c$; we used smoke to provide extra scatterers due to the low pulse energy ($\sim$1 pJ). A primary advantage of the SPAD camera is that it gives us both spatial information with resolution of the order of $\delta z = 1.6$ mm, and temporal information with resolution of the order of $\delta t = 110$ ps set by the impulse-response function of the SPADs. For each measurement, we typically collect 100 000 frames, each with an exposure time of 500 μs, resulting in a histogram of photon arrival times associated with each pixel, as shown in Figs. 5(b) and 5(c). These parameters

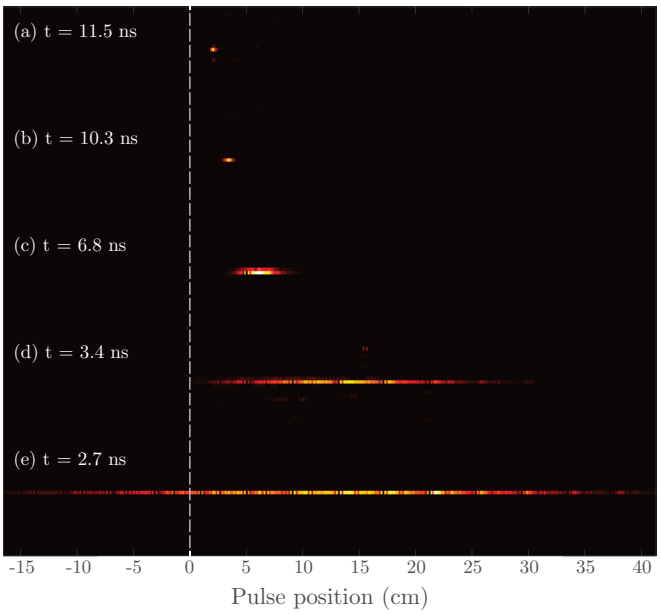

FIG. 2. Pulse compression for varying group velocity. The real time t is given for each pulse, with $t = 0$ ns corresponding to the time when the pulse enters the Rb vapor at $z = 0$ cm. The white dashed line denotes the position at which the light enters the Rb vapor. (a)–(d) correspond to group velocities of $v_g = c/183$, $c/81$, $c/24$, and $c/2.6$, with temperatures of $T \sim 150$, 130, 106, and 50 °C, respectively. (e) Pulse propagating through air to provide a reference for light traveling at $v_g \sim c$. See corresponding video in Supplemental Material [19] for the full pulse propagation. A 7 cm cell was used to obtain the higher temperatures necessary for (a) and (b), while a 30 cm cell was used for (c) and (d).

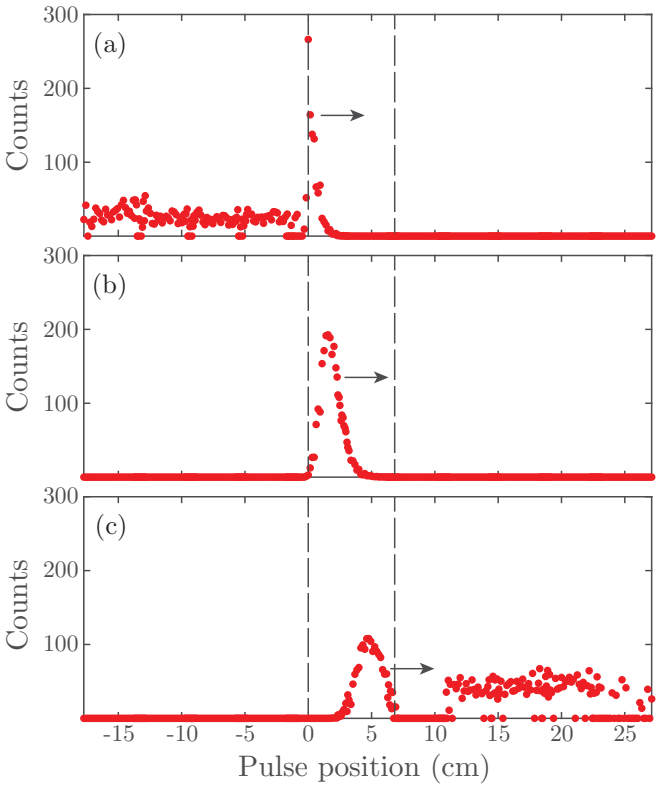

FIG. 3. Pulse compression. Subsequent frames show the pulse (a) propagating through air ($t = 2.96$ ns), (b) entering the heated Rb vapor cell ($L \sim 7$ cm) and compressing spatially due to the decrease in group velocity ($t = 5.01$ ns), and (c) exiting the cell and decompressing ($t = 8.19$ ns).

result in $\sim 7 \times 10^{-5}$ detected photons per pulse per pixel, well within the photon-starved regime, with $\sim 5 \times 10^{-6}$ detected photons per pulse per pixel corresponding to the signal from the nanosecond pulse and the rest due to continuous-wave (CW) leakage through the EOM integrated over the full 40 ns acquisition window (background CW flux of $\sim 1.6 \times 10^{-6}$ detected-photons/ns).

Our data processing steps are as follows. First, we subtract a background scan to account for any background photons due to light sources other than the laser. Second, we fit the histogram of photon arrival times associated with each pixel of the SPAD array with a Gaussian plus a constant offset that accounts for CW leakage from the EOM. We then subtract off the CW-leakage offset, and filter by the Gaussian FWHM τ and the signal-to-noise ratio (SNR), i.e., we set pixels to zero if they have low SNR or τ out of range. Last, for the data shown in Figs. 2 and 3, we replace each temporal histogram with its best-fit Gaussian.

V. PULSE COMPRESSION

A dramatic application of light-in-flight imaging is the *in situ* observation of pulse compression and slowing in the slow-light medium. Previous observations of slow light in Rb vapor have been limited to observing the net pulse delay at the output of the medium with respect to a reference pulse traveling through air. In contrast, light-in-flight imaging allows us to track the pulse propagation directly *inside* the medium, and to observe the spatial pulse compression as shown in Fig. 2. Ignoring dispersion (discussed in more detail in Sec. VII), the pulse temporal FWHM is independent of its group velocity, so the spatial extent of the pulse $\Delta z = v_g \tau$ must decrease as v_g decreases. Figures 2(a)–2(d) show the spatial extent of a pulse propagating with group velocities of $v_g = c/183$, $c/81$, $c/24$, and $c/2.6$, respectively, while Fig. 2(e) shows pulse propagation through air for comparison. All pulses are propagating from left to right. For a pulse propagating in air, $\tau = 1$ ns corresponds to $\Delta z = 30$ cm. Therefore, a group velocity of $v_g = c/183$ results in a pulse compressed to $\Delta z \sim 1.6$ mm. The time counters shown for each pulse correspond to the real time, with $t = 0$ ns corresponding to the time when the front edge of the pulse enters the Rb vapor at $z = 0$ cm, indicated by the dashed white line in Fig. 2. A full video of the pulse propagation for the range of v_g is provided in the Supplemental Material [19].

Figure 3 highlights the pulse compression as the light enters the Rb vapor. When a pulse enters the slow-light medium, the front edge of the pulse slows down, while the trailing end keeps moving forward at the speed of light. This results in a pulse pile up at the interface. Figure 3(a) shows the leading edge of the pulse entering the medium. Figure 3(b) shows the compressed pulse fully contained within the medium ($L \sim 7$ cm), and Fig. 3(c) shows the pulse exiting the cell and decompressing.

See the corresponding video in the Supplemental Material [19] for the full pulse propagation.

VI. SINGLE-PHOTON LAG TIME

In the following, we will show how by measuring the delay in arrival time of the scattered (single) photons, it is possible to extend the previous results to provide a measurement of the single-photon group velocity in the slow-light medium. In the photon-starved regime, the SPAD camera enables the observation of the *single*-photon group velocity, as demonstrated by Fig. 4. Figures 4(a) and 4(b) correspond to a set of scans taken with the camera at a single z position and falling Rb temperature, i.e., decreasing optical depth and increasing group velocity [20]. Figure 4(a) shows the pulse position along the beam path z plotted versus the scattered-photon arrival time t for three representative group velocities: $v_g \sim c/139$ [(iii), black diamonds], $c/41$ [(ii), blue circles], and $c/6$ [(i), red squares]. Here, t corresponds to the temporal location of the center of the histogram of scattered-photon arrival times recorded by a SPAD pixel located at position z. The pulse arrival times are determined as the peak position of the best Gaussian fit to the temporal histograms for each z position. Horizontal dashed lines correspond to the inner edges of the Rb vapor cell, where $z = 0$ corresponds to the position where the pulse enters the Rb vapor. Solid lines are fits $z = v_g(t - t_0)$ to the data, where v_g is the group velocity and t_0 is the time at which the pulse enters the cell. Note the time lag $t_0 \neq 0$, which corresponds to the time it takes the photons that are scattered by the medium to travel out of the cell ($\Delta x \sim r_{\text{cell}} \sim 1$ cm) as they propagate to the camera. Given the single-photon nature of the SPAD camera detection, the increase in scattered-photon arrival time t_0 with decreasing group velocity demonstrates that the slowing down of the group velocity observed for the main pulse propagating along the cell also applies to the single photons detected by the camera.

In Fig. 4(b), we plot the time lag t_0 versus measured group velocity v_g (black circles) for the full set of group velocities. For comparison, we plot the anticipated time lag $t_0 = r_{\text{cell}}/v_g$ (red solid line) assuming the pulse propagates down the center of the vapor cell, where $r_{\text{cell}} = 1.175$ cm is the inner radius of the vapor cell. The two curves are in good qualitative agreement and clearly in disagreement with the time lag $t_0 = r_{\text{cell}}/c = 0.04$ ns (blue dashed line) that one would expect if the scattered photons traveled out of the medium at the vacuum speed of light c. Figure 4(c) shows the difference in arrival time for photons scattered in the glass window at the entrance facet of the cell and the arrival time for photons scattered by the Rb vapor for pulse propagation at $v_g \sim c/183$. The photons scattered just after the pulse enters the Rb vapor arrive at the camera approximately 5.3 ns later than the photons scattered by the glass entrance window. Considering that the input pulse is 1 ns long, this last measurement provides direct visualization of a fractional delay for single photons of $f_D = \Delta t/\tau \sim 5$ over a propagation distance $\Delta x \sim 1$ cm, which is significantly higher than what can be achieved for single photons in EIT systems [1], and in keeping with a recent demonstration in a double-resonant configuration similar to that used here [4].

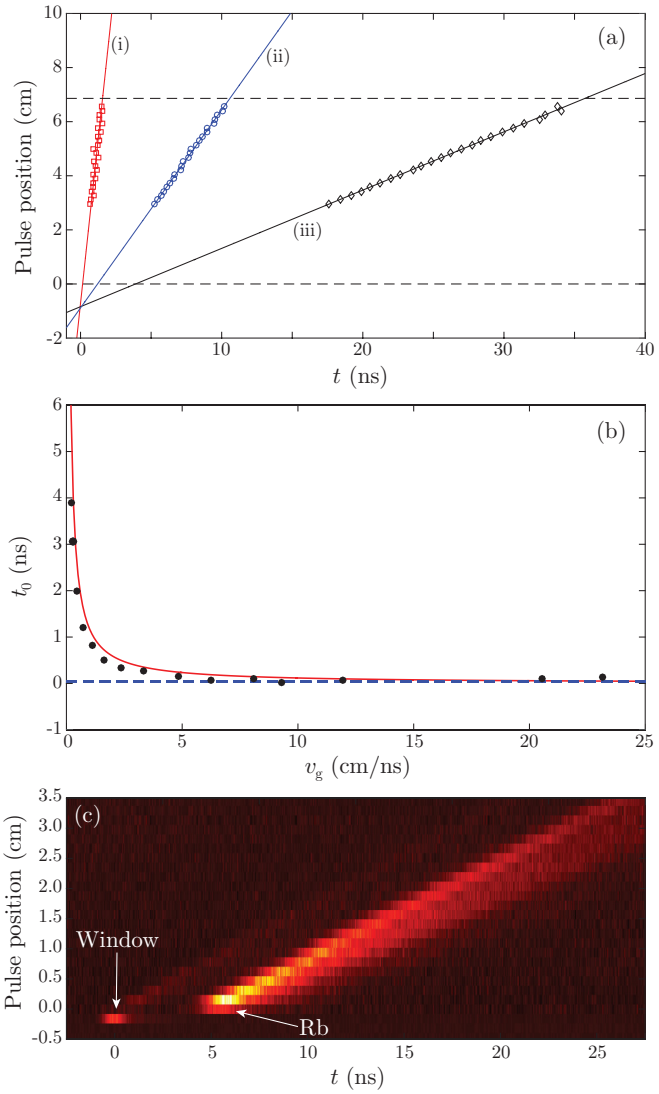

FIG. 4. (a) Representative plots of pulse position along the beam path z vs the scattered photon arrival time t, shown for group velocities $v_g \sim c/6$ [(i), red squares], $v_g \sim c/41$ [(ii), blue circles] and $v_g \sim c/139$ [(iii), black diamonds]. Horizontal dashed lines denote the inner edges of the Rb vapor cell, where $z = 0$ corresponds to where the pulse enters the Rb vapor. Solid lines are fits $z = v_g(t - t_0)$ to the data. (b) Photon-lag time vs group velocity. Black circles: extrapolated time t_0 at which the light entered the Rb vapor vs v_g. Red solid line: calculated time lag $t_0 = r_{\text{cell}}/v_g$, where $r_{\text{cell}} = 1.175$ cm is the inner radius of the vapor cell. Blue dashed line: time lag $t_0 = r_{\text{cell}}/c = 0.04$ ns that one would expect if the scattered photons traveled out of the medium at c. (c) Raw temporal profiles corresponding to each pulse propagation position for $v_g \sim c/183$. Note that the light scattered just after the pulse enters the Rb vapor arrives at the camera approximately 5.3 ns later than the light scattered by the glass window (indicated by white arrows).

VII. DISPERSION

Finally, we note that the light-in-flight technique also measures the pulse dispersion directly as a function of pulse propagation distance. Figure 5 shows pulse broadening and distortion for a $\tau \sim 1$ ns pulse traveling through the 30-cm-long Rb vapor cell, with $D \sim 0.92$ (Rb $T \sim 104\,^{\circ}$C) and

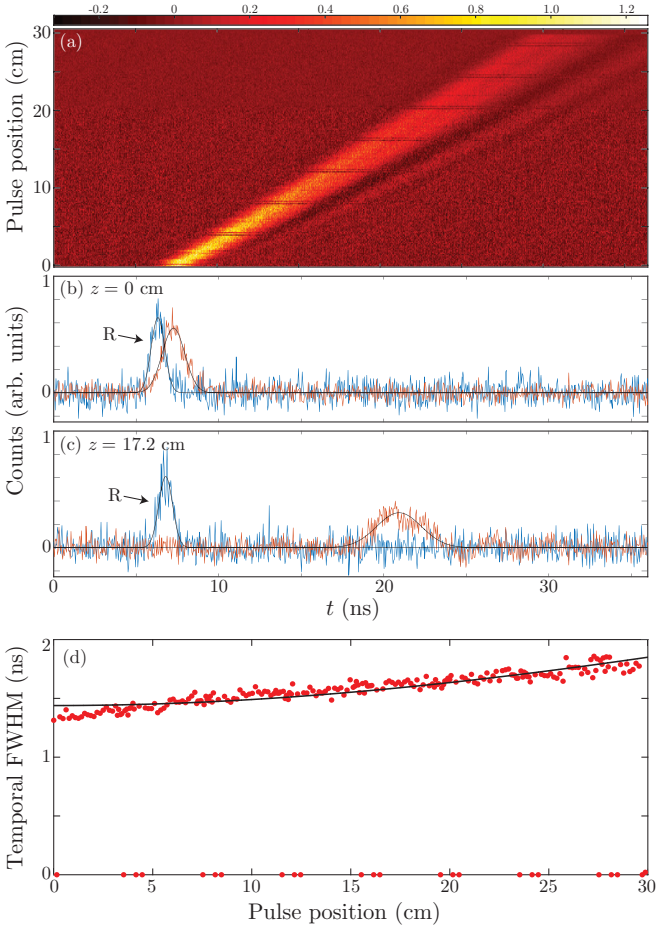

FIG. 5. Pulse dispersion observed for a pulse propagating through a Rb vapor cell of length $L = 30$ cm, with $v_g \sim c/24$ ($T \sim 104\,^{\circ}$C). (a) Plot of raw pulse temporal profiles (horizontal axis) for increasing propagation distance z (pulse position, vertical axis). (b),(c) Raw histograms and Gaussian fits to the temporal pulse profiles for $z = 0$ and $z = 17.2$ cm, respectively ($z = 0$ cm corresponds to the temporal pulse profile directly after it enters the Rb vapor). Blue traces, labeled R, correspond to a pulse in air for comparison. Relative amplitudes have been scaled (air: $N_{\text{counts}}/70$; Rb: $N_{\text{counts}}/200$) to allow for a comparison of the pulse shape. (d) Representative plot of pulse temporal FWHM τ vs pulse position z (red circles) for $T \sim 100\,^{\circ}$C, $D \sim 0.63$, and $v_g \sim c/13$. Solid black line: data fit with the function $\tau(z) = \sqrt{\tau_0^2 + (Bz/\tau_0^2)^2}$, where $\tau_0 = 1.44$ ns is the pulse FWHM at $z = 0$ and $\beta_3 = B/\sqrt{16[\ln(2)]^3} = 0.035$ ns^3/cm (see text). Noisy pixels, corresponding to the repeating line artifacts observed in (a), are set to $\sigma = 0$ and excluded from the fit shown in (d).

$v_g \sim c/24$. The orange traces in Figs. 5(b) and 5(c) show temporal profile line-outs taken from Fig. 5(a) at $z = 0$ and $z = 17.2$ cm, respectively. The blue traces, labeled R, show the temporal profile recorded for pulse propagation in air, and the relative amplitudes of the two traces have been scaled to allow for a comparison of pulse shape.

Pulse broadening due to pure quadratic dispersion should follow the form

$$\tau(z)^2 = \tau_0^2 + \left[\frac{4\ln(2)\beta_2 z}{\tau_0}\right]^2 + \left\{\frac{4[\ln(2)]^{3/2}\beta_3 z}{\tau_0^2}\right\}^2, \quad (6)$$

where τ_0 is the FWHM pulse width at $z = 0$ and

$$\beta_i = \frac{1}{c}\frac{d^i(\omega n'(\omega))}{d\omega^i}\bigg|_{\omega=(\omega_1+\omega_2)/2}, \quad (7)$$

where β_2 is the second-order contribution to the group velocity dispersion (GVD) and β_3 is the third-order dispersion coefficient [21]. For the atomic media in question, the third-order dispersion term dominates and we can ignore the effects of the second-order GVD. Here the third-order dispersion contributes to both pulse broadening, i.e., GVD, and pulse distortion, seen as intensity ripples on the leading edge of the temporal pulse profiles shown in Fig. 5(a) [5]. Figure 5(d) shows an example of the evolution of the temporal FWHM of the pulse as it propagates along z, for slow-light media with $v_g \sim c/13$ (Rb $T \sim 100\,^{\circ}$C, $D \sim 0.63$). The solid line is obtained by fitting the data to Eq. (6), setting $\beta_2 = 0$ and allowing τ_0 and β_3 to be parameters of the fit. The measured values of β_3 for the three decreasing group velocities $v_g = c/2.6$, $c/13$, and $c/24$ are $\beta_3 = 0.013$, 0.035, and 0.238 ns^3/cm, respectively, and increase as expected with increasing pulse slowing. We note that the quality of the fit decreases for slower group velocities, which we attribute to contributions from detuning-dependent absorption [5].

VIII. CONCLUSION

Single-photon light-in-flight photography allows direct visualization of the propagation of slow light in a hot atomic vapor. The technique provides direct evidence of pulse compression in space and of single-photon delays with fractional delays greater than 1 over ~1 cm of propagation. In particular, the absorption-doublet slow-light medium used here confirms that extremely large fractional delays are readily achievable with relatively large pulse bandwidths or short nanosecond-pulse durations, similar, for example, to those obtained from quantum-dot single-photon sources [4]. The same technique also reveals finer details such as pulse broadening in time due to the large dispersion associated with slow-light propagation. The results, on the one hand, highlight the utility of single-photon light-in-flight measurements for fundamental studies in slow-light media and, on the other hand, provide further support for the use of hot atomic vapors in future single-photon experiments and applications.

Open access data is available at Ref. [22].

ACKNOWLEDGMENTS

D.F. acknowledges financial support from the European Research Council under the European Union's Seventh Framework Programme (FP/2007-2013)/ERC, Grant No. GA 306559, and the Engineering and Physical Sciences Research Council (EPSRC, UK, Grants No. EP/M006514/1 and No. EP/M01326X/1). We thank ST Microelectronics, Imaging Division, Edinburgh for their support in the manufacture of the Megaframe chip. The Megaframe project has been supported by the European Community within the Sixth Framework Programme IST FET.

[1] M. D. Eisaman, A. Andre, F. Massou, M. Fleischhauer, A. S. Zibrov, and M. D. Lukin, Nature (London) **438**, 837 (2005).
[2] D. E. Chang, V. Vuletić, and M. D. Lukin, Nat. Photon. **8**, 685 (2014).
[3] R. M. Camacho, M. V. Pack, and J. C. Howell, Phys. Rev. A **73**, 063812 (2006).
[4] N. Akopian, L. Wang, A. Rastelli, O. G. Schmidt, and V. Zwiller, Nat. Photon. **5**, 230 (2011).
[5] R. M. Camacho, M. V. Pack, J. C. Howell, A. Schweinsberg, and R. W. Boyd, Phys. Rev. Lett. **98**, 153601 (2007).
[6] J. S. Wildmann, R. Trotta, J. Martín-Sánchez, E. Zallo, M. O'Steen, O. G. Schmidt, and A. Rastelli, Phys. Rev. B **92**, 235306 (2015).
[7] A. M. Marino, R. C. Pooser, V. Boyer, and P. D. Lett, Nature (London) **457**, 859 (2009).
[8] Z. Shi, R. W. Boyd, R. M. Camacho, P. K. Vudyasetu, and J. C. Howell, Phys. Rev. Lett. **99**, 240801 (2007).
[9] S. Franke-Arnold, G. Gibson, R. W. Boyd, and M. J. Padgett, Science **333**, 65 (2011).
[10] A. Safari, I. De Leon, M. Mirhosseini, O. S. Magaña-Loaiza, and R. W. Boyd, Phys. Rev. Lett. **116**, 013601 (2016).
[11] P.-C. Kuan, C. Huang, W. S. Chan, S. Kosen, and S.-Y. Lan, Nat. Commun. **7**, 13030 (2016).
[12] J. Dressel, S. G. Rajeev, J. C. Howell, and A. N. Jordan, Phys. Rev. A **79**, 013834 (2009).
[13] R. W. Boyd, D. J. Gauthier, A. L. Gaeta, and A. E. Willner, Phys. Rev. A **71**, 023801 (2005).
[14] I. Novikova, D. F. Phillips, and R. L. Walsworth, Phys. Rev. Lett. **99**, 173604 (2007).
[15] Y.-H. Chen, M.-J. Lee, I. Chung Wang, S. Du, Y.-F. Chen, Y.-C. Chen, and I. A. Yu, Phys. Rev. Lett. **110**, 083601 (2013).
[16] G. Gariepy, N. Krstajić, R. Henderson, C. Li, R. R. Thomson, G. S. Buller, B. Heshmat, R. Raskar, J. Leach, and D. Faccio, Nat. Commun. **6**, 6021 (2015).
[17] J. Richardson, R. Walker, L. Grant, D. Stoppa, F. Borghetti, E. Charbon, M. Gersbach, and R. Henderson, in *Proceedings for IEEE 2009 Custom Integrated Circuits Conference (CICC)* (IEEE, 2009), p. 77.
[18] J. Richardson, L. Grant, and R. Henderson, IEEE Photon. Tech. Lett. **21**, 1020 (2009).
[19] See Supplemental Material at http://link.aps.org/supplemental/10.1103/PhysRevA.95.023830 for movies showing the full pulse propagation corresponding to the frames shown in Figs. 2 and 3 in the main text. Movie1 corresponds to Fig. 2 and shows the relative pulse compression for pulses propagating at different group velocities. Movie2 corresponds to Fig. 3 and shows the pulse compression observed as the pulse enters the slow light medium, and subsequent decompression when the pulse exits the medium.
[20] For the data shown in Figs. 4(a) and 4(b), the EOM pulse (25 MHz, 8% duty cycle) was fed into a tapered amplifier resulting in pulse energies ∼30 nJ, with $\tau \sim 3.2$ ns. We used an exposure time of 5 μs resulting in $\sim 5 \times 10^{-4}$ detected photons per pulse per pixel corresponding to the pulse signal and $\sim 3 \times 10^{-3}$ photons per pulse per pixel due to CW leakage through the EOM (background CW flux of $\sim 7.5 \times 10^{-5}$ detected-photons/ns integrated over the full 40 ns acquisition time).
[21] G. Agrawal, *Nonlinear Fiber Optics*, 3rd ed. (Academic, San Diego, 2001).
[22] doi:10.17861/88bf95e1-eb30-4bcc-8b44-e6098bbbcfed.